

www.lpr-journal.org

# A MHz—Level Swept Source by Time Stretching the Shot—Noise Limited Supercontinuum Based on a Mode—Locked Laser and the Application in Optical Coherence Tomography

Laiyang Dang, Wenhao Zhu, Shuyuan Zhu, Yujia Li, Yihuan Shi, Qian Li, Feng Li, and Dongmei Huang\*

The performance of swept—source optical coherence tomography (SS—OCT) is fundamentally limited by a critical trade-off between achievable imaging range and imaging speed. Current supercontinuum broadening swept source is usually above tens of MHz, which severely restricts the detection distance and application scope of the SS-OCT system. Here, a MHz-level mode-locked laser supercontinuum-based SS-OCT is first presented, with an axial resolution of 11.4 µm and a long imaging range with a 6 dB sensitivity roll-off length of 119 mm. A low-repetition-rate mode-locked laser with 5.7 MHz is built as the seed laser based on low-nonlinear large-mode-area fiber (LMAF), which is then used to achieve low-noise and high-coherence spectral broadening through all-normal dispersion (ANDi) fiber. A single-pulse operation with long-term stability and self-starting can be achieved without any active feedback control. Notable, the average cross-correlation coefficient between different scanning cycles is as high as 0.997, and the coefficient of variation (CV) is 0.074%, indicating that the constructed swept source has excellent repeatability and high coherence. This work demonstrates the possibility of generating the low-repetition-rate mode-locked laser and MHz swept laser with high coherence and low noise characteristics, which contributes to the development of ultrafast laser and applications of SS-OCT.

# 1. Introduction

Swept lasers are widely used in optical fiber sensing,[1] laser metrology,[2] optical coherence tomography (OCT),[3,4] and light detection and ranging (LiDAR).[5,6] In general applications, wide sweep range, high sweep rate, and narrow instantaneous linewidth are the most desirable features for a swept laser. In a swept source OCT (SS-OCT) system, the above three parameters of the swept laser directly determine the axial resolution, axial sweep rate, and the sensitivity roll-off length of the SS-OCT system, respectively. The development of high-speed SS-OCT system is significant for the development of real-time imaging technology. Here, considering the trade-off between imaging range and speed, a MHz-level swept source with wide swept range is desirable for realizing high-speed SS-OCT and long imaging range.<sup>[7,8]</sup>

The traditional swept laser takes a long time to build up laser signal during

L. Dang, W. Zhu, S. Zhu, Y. Shi, D. Huang Photonics Research Institute Department of Electrical and Electronic Engineering The Hong Kong Polytechnic University Hong Kong, Hong Kong E-mail: meihk.huang@polyu.edu.hk

The ORCID identification number(s) for the author(s) of this article can be found under https://doi.org/10.1002/lpor.202500743

© 2025 The Author(s). Laser & Photonics Reviews published by Wiley-VCH GmbH. This is an open access article under the terms of the Creative Commons Attribution-NonCommercial-NoDerivs License, which permits use and distribution in any medium, provided the original work is properly cited, the use is non-commercial and no modifications or adaptations are made.

DOI: 10.1002/lpor.202500743

L. Dang, W. Zhu, Y. Shi, F. Li, D. Huang The Hong Kong Polytechnic University Shenzhen Research Institute Shenzhen 518057, China

Y. Li

The Key Laboratory of Optoelectronic Technology & Systems (Education Ministry of China)
Chongqing University
Chongqing 400044, China

Q. Li

School of Electronic and Computer Engineering Peking University Shenzhen 518055, China



www.advancedsciencenews.com

& PHOTONICS REVIEWS

www.lpr-journal.org

wavelength scanning, which limits the swept speed. To weaken the limit of laser rebuilding time in conventional swept laser with an intracavity swept filter, researchers use different combinations to reduce the cavity length. An integrated external cavity diode laser with a cavity length of a few centimeters could obtain swept signals with >200 KHz repetition rate, [9] but the mode separation of a few GHz is relatively large. Sampled-grating distributed Bragg reflector diode laser could further reduce the cavity length to <1 mm,[10] but the wavelength sweep should be realized by Vernier tuning of multiple semiconductor sections, which is hard for massive production. MEMS-VCSEL avoids the Vernier tuning by reducing the cavity length to the magnitude of ≈10 micrometers and enhances the FSR to >10 THz, [11,12] but its output power is too low and the linewidth is also large because of the low-quality cavity. In contrast to reducing the cavity length, another scheme with a long fiber cavity, which is named as Fourier domain mode locked (FDML) laser,[13,14] has also shown good performance to obtain high repetition rate of wavelength scanning. However, it is extremely hard to obtain a stable output from FDML lasers.

The forementioned swept lasers suffer from different imperfections such as random mode hopping, discontinuous tuning current, low cavity quality, cavity mismatch and nonlinearity induced instabilities, and large phase or frequency noise are introduced into the swept signals and degrade the stability of the sweep traces. The fundamental or intrinsic reason of the low coherence is the weak phase relationship between the laser signals at different wavelengths in the full sweep range. To benefit from the highly coherent mode locked lasers, which have strong predictable phase relationships between the different wavelengths in the full spectrum, a time stretching technique to generate a highly chirped pulse from a broadband ultrashort pulse has been proposed.[15-17] Generation of highly coherent broadband spectra can be obtained in short cavity mode locked fiber laser cavities with schemes including nonlinear polarization rotation (NPR),[18,19] Figure-of-eight,[20-22] and Figure-of-nine, [23,24] which has tens of megahertz repetition rate. To mitigate the huge gap between the requirement of low repetition rate and the available high ones, we have previously proposed a pulse picker technology to reduce the repetition rate of a broadband femtosecond pulse train from 100 MHz to 2.5 MHz by a Mach–Zehnder intensity modulator, [25] whose output power is attenuated by more than 20 dB and leads to a low signal to noise ratio in the SS-OCT system. A MHz level low repetition rate broadband femtosecond pulse train is highly desirable to generate a highly coherent MHz–level swept source.

The major difficulty to build a low repetition rate femtosecond mode locked fiber laser comes from the accumulation of non-linearity and higher order dispersion distortion in the long fiber cavity, the complicated nonlinear dynamics in such cavities could lead to multi–pulsing, pulse splitting or breathing, and even a noise like pulse train, which will deteriorate the coherence and narrow the spectrum of the mode locked pulse.<sup>[26–28]</sup> At present, the most widely used scheme is to employ a narrowband filter to remove the nonlinear chirp of the pulse edge and increase the pulse width, thereby reducing the influence of nonlinear phase shift and preventing optical wave—breaking (OWB).<sup>[29–31]</sup> However, the spectrum is less than 1 nm, which will seriously affect the subsequent spectrum broadening. In addition, it is difficult

for long cavity laser to self-start, which will seriously limit its application in OCT systems.<sup>[32]</sup> Another key point is to further expand the spectral bandwidth to improve the measurement resolution. Recently, the invention of supercontinuum technology has made it possible to generate ultra-broadband pulsed lasers.[33-35] However, these conventional supercontinuum sources have low coherence due to severe intensity noise/pulse-to-pulse relative jitter. To ensure high coherence, low noise and flat spectrum laser, high nonlinearity and all-normal dispersion (ANDi) media can be pumped with short-duration pulses of high peak power.[36-38] This broadening mechanism includes self-phase modulation (SPM) and coherent OWB, which ultimately achieves a highly coherent, flat and broadband spectrum that can be used for SS-OCT with long imaging range and high resolution. Grelet et al. has demonstrated an ANDi supercontinuum source using short pump pulses and applied it to spectrum domain OCT system with less than 1 mm imaging range, [39] and the repetition rate is up to 40 MHz. Up to now, MHz level broadband pulses are still not available, let alone stretched swept laser with MHz swept rate and broadband swept range.

In this work, we propose and demonstrate a 5.7 MHz low-repetition-rate all-fiber mode-locked laser with 6.1 nm broadband spectrum, high stability and self-startability. By introducing a large-mode-area fiber (LMAF) to increase the cavity length and place it between two sections of dispersion compensation fiber (DCF) with lower pulse energy, the nonlinear phase shift is effectively attenuated to maintain single pulse state. Subsequently, ANDi supercontinuum dynamics is studied to achieve low-noise and high-coherence spectral broadening with more than 120 nm bandwidth. The distribution of energy and spectral correlations over the full pulse period is statistically analyzed by capturing the single-shot spectrum of the supercontinuum source. The relative intensity noise (RIN) of the laser is measured to be as low as -128 dB/Hz. A high-performance swept source is realized by time-stretching the supercontinuum broadband femtosecond pulse train. Applying this high performance swept laser to SS-OCT system, an axial resolution of 11.4 µm and a 6 dB sensitivity roll-off length of up to 119 mm with A-scan rate of 5.7 MHz is achieved, which is the first time to present the state-of-the-art supercontinuum source for SS-OCT system. This highly coherent and stable swept laser with more than 100 nm sweep range and MHz level sweep rate will boost the advancement of high resolution, high speed and long-distance detection systems including SS-OCT, OFDR, and LiDAR, which is beneficial for the medical diagnose, industrial inspection and driverless technology.

# 2. Experimental Setup

#### 2.1. Low Repetition Rate Supercontinuum-Based Swept Source

The experimental setup of the low repetition rate supercontinuum—based swept source is shown in **Figure 1**. Part I shows the schematic of a low—repetition—rate mode—locked fiber ring laser based on non—linear polarization rotation (NPR) mode—locking technique,<sup>[40]</sup> which will be used as the seed signal to generate broadband supercontinuum. Compared with other mode—locking mechanisms, NPR has a high damage threshold, strong self—starting ability, and a wide spectral

-and-conditions) on Wiley Online Library for rules of use; OA articles are governed by the applicable Creative Commons

www.advancedsciencenews.com

& PHOTONICS REVIEWS

www.lpr-journal.org

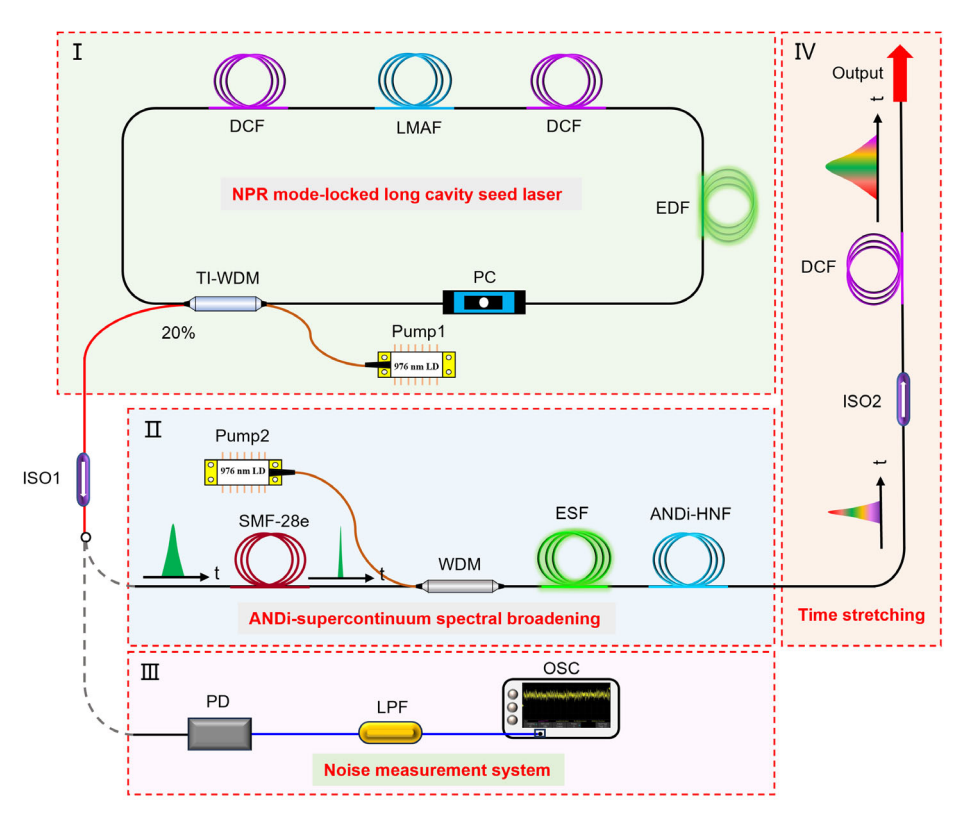


**Figure 1.** Experimental setup of the time-stretched swept source induced by low repetition rate mode-locked laser and supercontinuum broadening. EDF, erbium-doped fiber; DCF, dispersion compensation fiber; LMAF, large-mode-area fiber; TI-WDM, tap-isolator wavelength division multiplexer; PC, polarization controller; ISO, isolator; SMF, single-mode fiber; ESF, erbium-doped photosensitive fiber; ANDi-HNLF, all-normal dispersion-highly nonlinear fiber; PD, photodetector; LPF, low-pass filter; OSC, oscilloscope.

bandwidth. A segment of 0.5-m Erbium-doped fiber (EDF, Er80-8/125, Liekki) with a dispersion of  $\approx$ 16.14 ps nm<sup>-1</sup> km<sup>-1</sup> at 1550 nm is pumped by a 976 nm laser diode. The laser configuration is simplified by a multifunctional integrated module for tap/isolator/wavelength division multiplexer (TI-WDM). About ≈30 m LMAF (Yangtze Optical Fibre, G.654) with a dispersion of ≈21 ps nm<sup>-1</sup> km<sup>-1</sup> and a nonlinear coefficient of 0.56 W<sup>-1</sup>km<sup>-1</sup>at 1550 nm is utilized to reduce the intracavity nonlinearity. Two sections of 2-m DCF with a dispersion of -166.1 ps nm<sup>-1</sup>km<sup>-1</sup> are used to compensate for the cavity dispersion close to near-zero normal dispersion. Besides, the DCFs are spliced before and after the LMAF to control the nonlinearity of the LAMF and reduce the pulse energy. The mode locking is achieved by adjusting the polarization state and controlling the nonlinearity through the polarization controller (PC). An isolator (ISO1) is placed at the 20% output port to avoid affecting the seed source by blocking the external reflected light. Part II presents the schematic of the ANDi supercontinuum spectra broadening system. The seed signal is injected into a 9-m single-mode fiber (SMF-28e) with a dispersion of  $\approx 17$  ps nm<sup>-1</sup> km<sup>-1</sup> at 1550 nm to achieve pulse compression. The pulse peak power is amplified by utilizing a 1.5-m Erbium-doped photosensitive fiber (SM-ESF-7/125, Nufern)-based self-built amplifier with high conversion efficiency. A 0.45 m highly nonlinear fiber (HNLF, NL-1550-NEG) with a dispersion of -5 ps nm<sup>-1</sup>km<sup>-1</sup> and a nonlinear coefficient of 10 W-1km-1 is used to generate the low noise supercontinuum. The noise measurement system in Part III consists of a photodetector (PD, Max-ray Photonics,) with a bandwidth of 3 GHz, an electrical low-pass filter (LPF) with a bandwidth of 7 MHz, and an oscilloscope (OSC1, RIGOL, HDO4804) with a bandwidth of 800 MHz. Time stretching is actually an analogy of paraxial diffraction (Fraunhofer diffraction) and time domain dispersion, which is a crucial technique to generate a chirped pulse with help of dispersion. Time stretching technology can not only generate swept signals, it also is an effective way to break through the speed limitation of traditional spectrometers, thus enabling fast real-time spectroscopy measurements. The time stretched swept source is shown in Part IV. A one-to-one mapping relationship is formed between the spectral domain and the time domain when the stable phase approximation condition is satisfied by effective dispersion. Due to the long pulse period, a 6.5 km DCF is used to provide large group velocity dispersion (GVD) to increase the pulse duration.

# 2.2. SS-OCT System

**Figure 2** shows the schematic diagram of the SS-OCT system with a sweep rate of 5.7 MHz. 10% of the swept source from optical coupler (OC1, 10:90) is detected by the PD and used as a trigger to collect the interference signal. The remaining 90% of

www.advancedsciencenews.com

LASER & PHOTONICS REVIEWS

www.lpr-journal.org

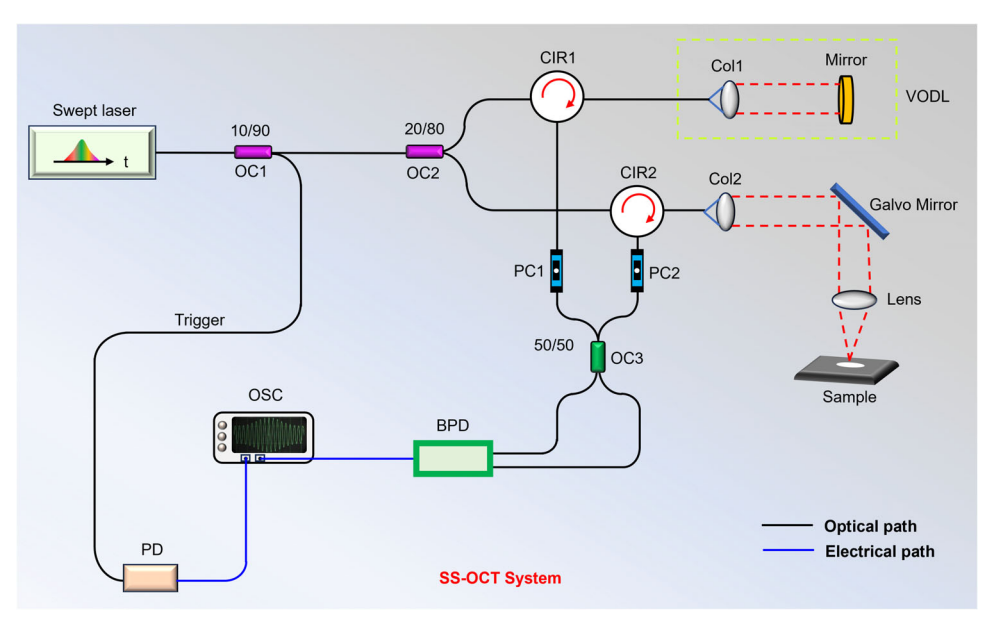


Figure 2. Schematic diagram of the SS-OCT system. OC, optical coupler; CIR, circulator; Col, collimator; VODL, variable optical delay line; PC, polarization controller; PD, photodetector; OSC, oscilloscope; BPD, balanced photodetector.

the swept source is further split into two parts by a 20:80 OC2 and injected into the two arms of the Michelson interferometer. 20% of the swept signal propagates to reference arm, which consists of a circulator (CIR1), a variable optical delay line (VODL) and a collimator (Col1), and a motorized mirror. The light from the 80% port is input into CIR2 and then focused onto the sample placed on the stage by a collimator (Thorlabs, LA1509-C) and a scanning galvo mirror (Thorlabs, GVS102). The galvo scanning system is driven by a sinusoidal electrical signal with a scanning speed of 500 Hz generated by an arbitrary waveform generator (160 MHz dual-channel capability, BK PRECISION). The polarization states of the optical signal in both arms are adjusted by two squeeze polarization controllers (PC1 and PC2) to achieve an optimal interference pattern. Then, the reflected lights from the sample and reference arms are combined by a 2×2 50:50 OC3. The interference signal is detected by a balanced photodetector (Finisar, BPDV3120R) with a bandwidth of 70 GHz and acquired by a real-time oscilloscope (OSC2, Tektronix, DPO77002SX ATI) with a bandwidth of 70 GHz and a sampling rate of 200 GSa  $s^{-1}$ .

# 3. Experimental Results and Discussion

#### 3.1. Low Repetition Rate Mode-Locked Laser

The nonlinear distortion accumulated in the long fiber delay line will be the first dominant barrier that will induce instability, pulse breaking and nonlinear chirp to the lasing pulse. Therefore, in the proposed laser cavity, we utilized LAMF with relatively low nonlinearity compared with SMF-28e. Besides, we also control and optimize the pump power with 50 mW to obtain a stable single pulse output. Furthermore, polarization state in the laser cavity is carefully adjusted to ensure NPR mode−locking operation. The average spectrum is measured by an optical spectrum analyzer (OSA, Yokogawa AQ6370D) as shown in **Figure 3**a, where a flat spectrum has a 3 dB bandwidth of about ≈6.1 nm. It is

challenging to further broaden the spectrum directly from the mode locked laser due to the nonlinearity and the cross-phase modulation generated in the cavity causing short wavelengths to produce interferometric patterns. The pulse interval as shown in Figure 3b is 173.37 ns, which is consistent with the round-trip time of the laser cavity length. Here, the pulse intensity fluctuation is caused by its high-frequency components exceeding the bandwidth limit of the oscilloscope, resulting in the attenuation or inability to fully capture the high-frequency components of the signal. [41] The signal-to-noise ratio (SNR) is as high as 92.4 dB measured with a resolution of 1 Hz and a range of 30 kHz as shown in Figure 3c, indicating stable mode locking operation. The inset shows the higher harmonics with a resolution of 1 kHz and a range of 100 MHz, and no noise spikes are observed. Furthermore, no intensity fluctuation is observed in the RF spectrum, also indicating the good stability of the pulse sequence. In addition, pulse width is 1.259 ps as shown in Figure 3d by the hyperbolic secant fitting of the autocorrelation trace, achieving a time-bandwidth product of 0.96. Therefore, there is a large chirp in the pulse, which can be compressed to the femtosecond level outside the cavity.

The proposed laser system alternately contains two dispersive elements, normal and anomalous, and the net dispersion in the cavity is close to zero. The resulting pulse will experience a large broadening and compression in the laser cavity, which effectively reduces the peak power of the pulse and alleviates the limitation of the nonlinear effect on the pulse energy. When operating in the extended pulse state, low nonlinear fiber is introduced to further reduce the amount of nonlinear phase  $\varphi_{NL}$  accumulated in each round trip to prevent multi–pulse splitting. Since  $\varphi_{NL}$  is proportional to the  $P_0L$  (where L is the cavity length and  $P_0$  is the peak pulse power), [42] increasing the cavity length to reduce the repetition rate requires a corresponding reduction in the peak pulse power to keep the sum of the nonlinear phases per round trip from exceeding the split—limiting phase, i.e.,  $\varphi_{NL} < \pi$ . Therefore,

(a)

Intensity (dB)

(c)

Intensity (dB)

5.76

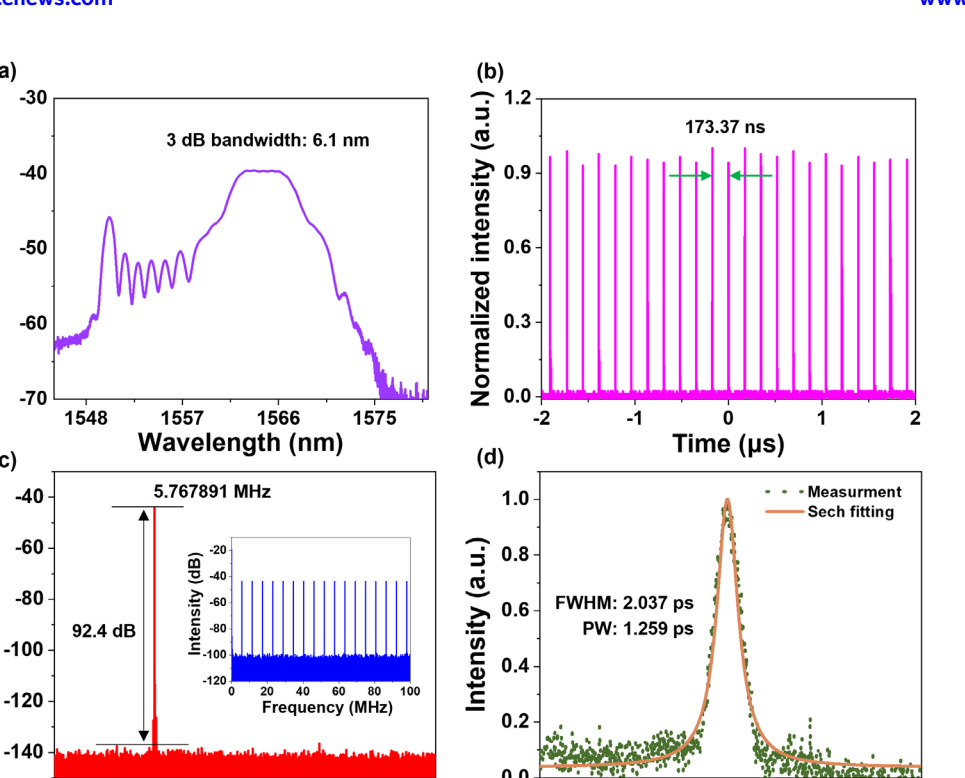


Figure 3. Output pulse characteristics of the low-repetition-rate mode-locked fiber laser, a) Optical spectrum. b) Pulse sequence, c) Measured RF spectrum of pulse sequence with a resolution of 1 Hz, with the inset showing the higher harmonics; d) Measured autocorrelation trace and fitting trace.

it is necessary to study the existence state of solitons in the laser cavity under various pump powers to master the law of the long cavity laser. Here, the pump power is increased from 0 to 100 mW in steps of 1 mW. Figure 4a shows a 2D pseudo-color image of the optical spectrum evolution, from which it can be seen that in the locked mode state, the spectral energy increases by adjusting the pump power upward, and its shape evolves periodically. Besides, the time domain pulse also has a rich output state as the power increase as shown in Figure 4b. From the above results, it can be inferred that the laser went through four stages: amplified spontaneous radiation (ASE: 0-41 mW), continuous wave (CW: 42-47 mW), single pulse (SP: 48-58 mW) and multi-pulse (MP: 59-100 mW). The sought-after result is single pulse operation to serve as a seed source for supercontinuum generation. Here, the long cavity has a large nonlinear effect, so the laser can maintain a single pulse state only within a short pumping power interval. In addition, when the pump power is further increased to 58 mW, mode-locked pulse and CW will coexist as shown in Figure 4c. The reason is that as the pump power increases, due to the soliton energy saturation effect, the laser will transfer the excess energy to the CW to stabilize the single soliton mode locking when the soliton is pumped above a certain threshold. The direct current component in the spectrum disappears when the pump power is increased to 59 mW, as shown in Figure 4d. The corresponding pulse sequence is shown in Figure 4e, where the intra-cavity pulse is split into two solitons. At this moment, the energy in the cavity exceeds the upper limit of a single pulse, the accumulated large nonlinear effect in the laser system causes pulse splitting.

5.77

5.78

Frequency (MHz)

Due to the balance between nonlinear effect and dispersion effect, the soliton splitting spectral characteristics remain constant. Figure 4f shows the pulse train of the laser when the pump power is 100 mW, where the pulses split into many soliton forms and the spectra remain intact.

Time (ps)

10

Figure 5a shows the relationship between the output power of the seed laser and the pump power, and the output power of the laser during the single pulse operation is 300  $\mu W$  to 500  $\mu W$ . The single pulse energy of the laser output in the SP state can reach up to 88.7 pJ, and the corresponding pulse peak energy is as high as 69.7 W. The corresponding accumulated nonlinear phase shift in the laser cavity is calculated to be 2.126. These results indicate that the insertion of LMAF can effectively reduce the accumulation of nonlinearity in the cavity and achieve high performance and low weight mode-locked frequency laser output. In addition, the RIN of the laser at different pump powers are characterized to further study the stability of the laser output power, as shown in Figure 5b. Benefiting from the dispersion management in the cavity, the RIN as low as  $-125 \text{ dB Hz}^{-1}$  is achieved over the high spectral range at a pump of 50 mW. We further calculated the integrated RINs at different pump powers, where the integrated noise level deteriorates with increasing pump power and is significantly affected by low-frequency noise. In addition, we also calculated the corresponding root mean square (RMS) values of the integrated RINs to be 76 ppm, 105 ppm, and 128 ppm (ranging from 100 Hz to 1 MHz), which gives outstanding results in a free-running mode-locked all-fiber laser without any active suppression of the RIN. The increasement of pump power leads to

18638899, 0, Downloaded from https://onlinelibrary.wiley.com/doi/10.1002/por.202500743 by HONG KONG POLYTECHNIC UNIVERSITY HUNG HOM, Wiley Online Library on [30092025]. See the Terms and Conditions (https://onlinelibrary

conditions) on Wiley Online Library for rules of use; OA articles are governed by the applicable Creative Commons License

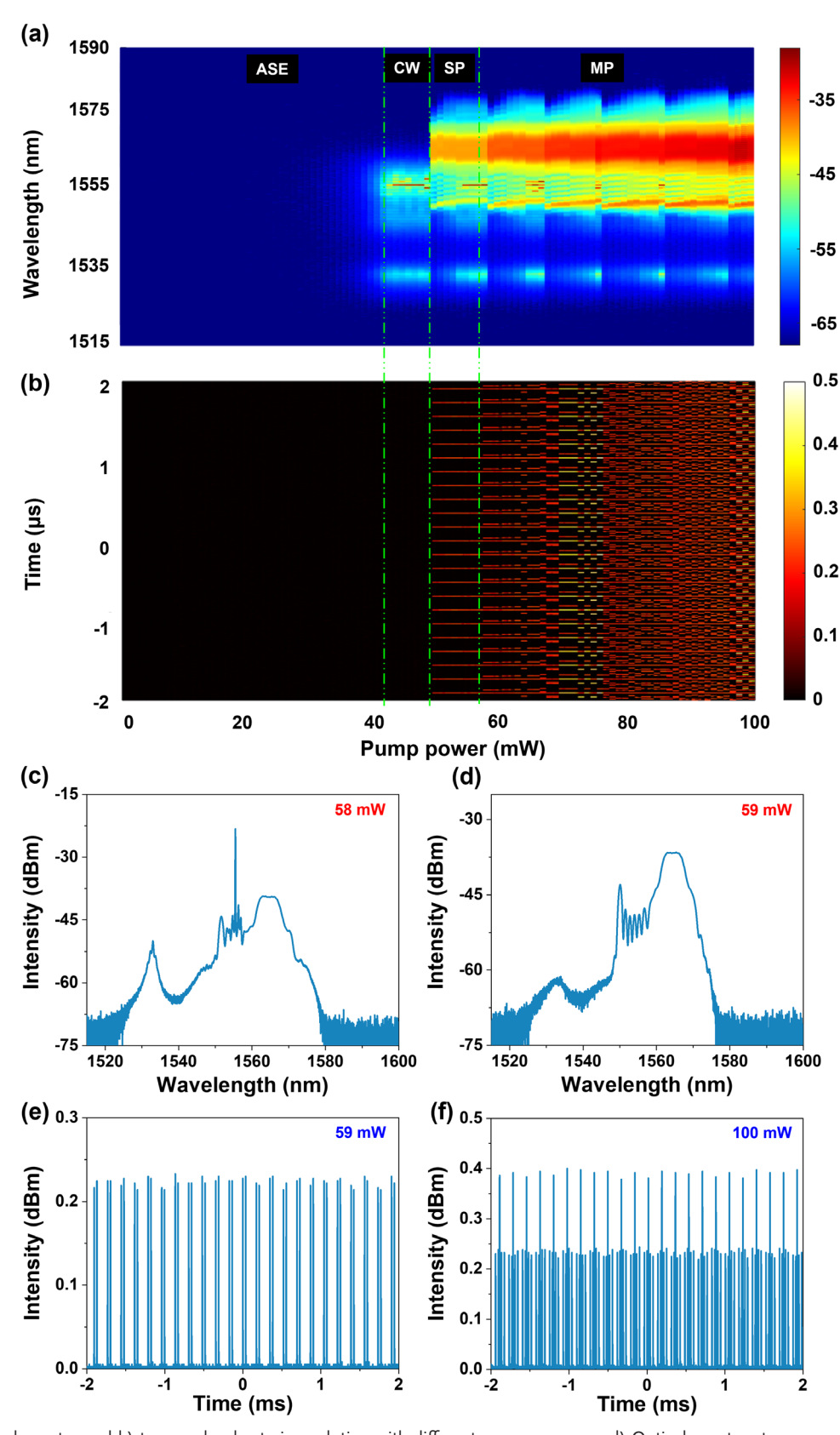


Figure 4. a) Optical spectra and b) temporal pulse train evolution with different pump powers. c,d) Optical spectra at pump powers of 58 mW and 59 mW, respectively. Typical pulse trains at pump powers of e) 59 mW and f) 100 mW.

18638899, 0, Downloaded from https://onlinelibrary.wiley.com/doi/10.1002/por.202500743 by HONG KONG POLYTECHNIC UNIVERSITY HU NG HOM, Wiley Online Library on [30.09/2025]. See the Terms

conditions) on Wiley Online Library for rules of use; OA articles are governed by the applicable Creative Commons

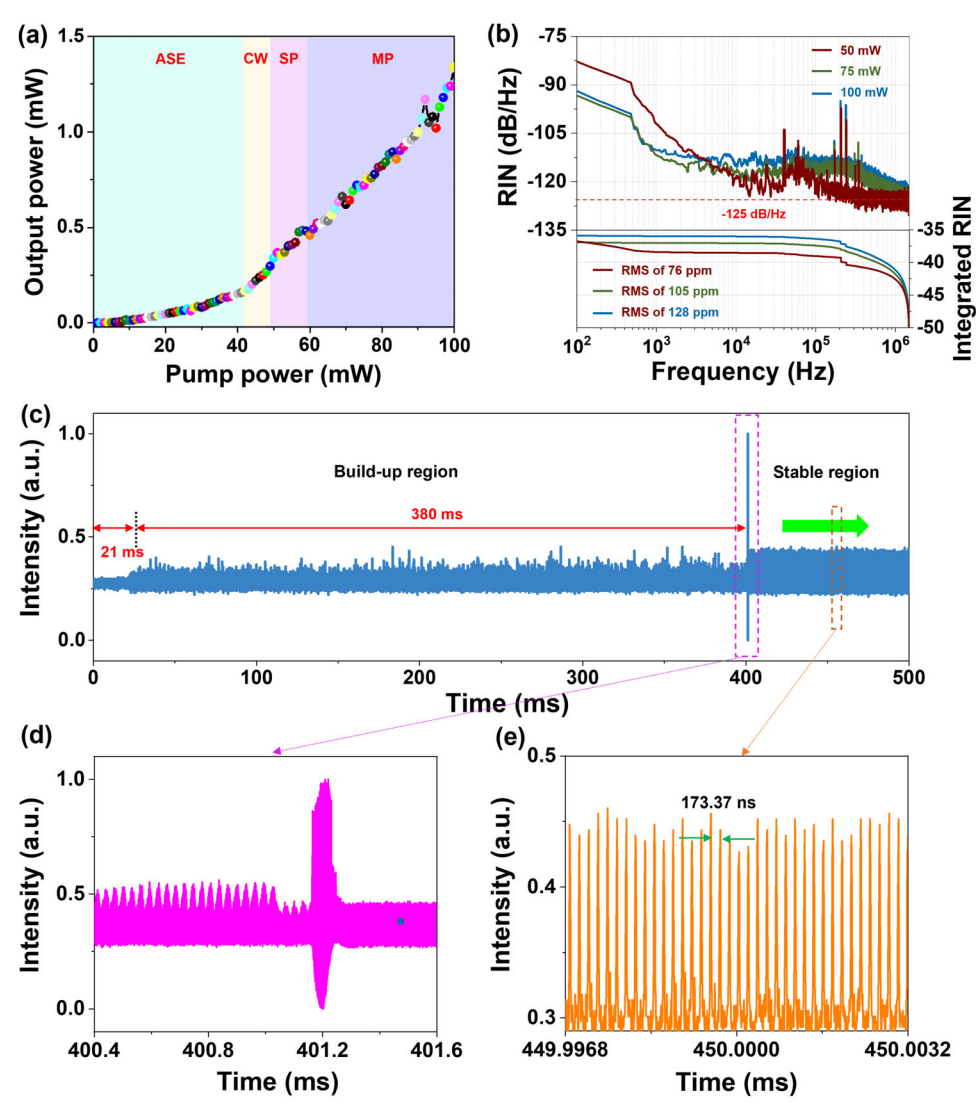


Figure 5. a) Output power of the mode—locked fiber laser versus the pump power. b) Measured RIN spectra and integrated RINs of the laser from 100 Hz to 1 MHz Fourier frequency at different pump powers. c) Real-time measurement of the self—starting process of a single soliton state in a long—cavity fiber laser. d) Pulse sequence around the Q-switched giant pulse appears. e) Pulse sequence of laser output after stable mode—locking.

multi-pulse operation and deteriorates the high-frequency RIN of the laser. The reason is that pulse splitting will introduce additional frequency components and phase changes, which will lead to large power jitters and instability. The long fiber cavity is susceptible to quantum noise and thermal noise, which will destroy the equilibrium state of the reverse population in the gain medium and cause the disturbance of the excited radiation energy in the cavity, resulting in relaxation oscillation and noise peak. Therefore, obvious noise peaks are observed near the frequency offset of 39-206 kHz. At a pump power of 50 mW, self-starting single-pulse mode-locking operation is realized by carefully adjusting the PC. The pulsing dynamics from the CW state to the single soliton output is shown in Figure 5c, and a long cavity mode-locking process of up to 401 ms is observed for the first time. Notably, the laser exhibits rich dynamic behaviors after the pump is turned on. The laser remains in relatively stable CW state for the first 21 ms and generates relatively weak Q-switched

pulses in the following 380 ms.  $^{[43]}$  The high peak power pulse evolves into a stable mode—locked pulse within a time interval of < 90.8  $\mu$ s after generating a giant Q—switched pulse, as shown in the enlarged Figure 5d. Figure 5e shows a pulse train around 450 ms. The time interval is 173.37 ns, which is consistent with the result in Figure 3d, indicating that the laser can automatically enter a stable SP mode—locked state.

To comprehensively explore the long—term stability of the proposed long—cavity mode—locked fiber laser system during continuous operation, the optical spectra and RF spectra are obtained at 5—second intervals within a 90—min period, as shown in **Figure 6**. The stability test is performed on the laser system in a natural environment while maintaining the free running operation. No obvious optical spectral fluctuations are observed during the 90—min experiment, as shown in Figure 6a. Figure 6b shows the evolution of the corresponding central wavelength, output power, and 3 dB bandwidth. The standard deviation (SD) of the

LASER & PHOTONICS

www.advancedsciencenews.com

www.lpr-journal.org

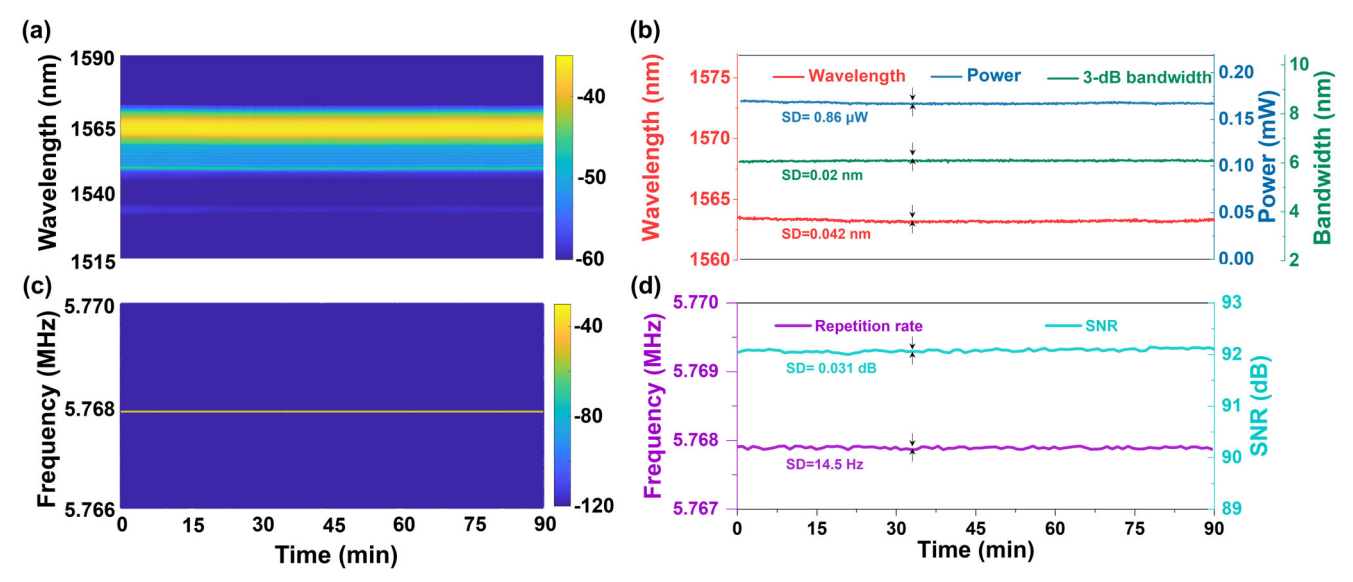


**Figure 6.** Long-term robustness of the single—pulse state over 90 min of continuous operation. a) Temporal evolution of the measured optical spectrum. b) Stability performances of the lasing wavelength, output power, and 3 dB bandwidth. c) RF spectrum scanned repeatedly every 5 s. d) Fluctuation of the repetition rate and SNR.

central wavelength fluctuation is 0.042 nm, the SD of the output power disturbance is 0.86  $\mu W$ , and the 3 dB bandwidth of the output spectrum is all more than 6 nm. The SD of the disturbance is 0.02 nm. Figure 6c shows the 2D pseudo–color graph of the evolution of the RF spectrum over time, from which no obvious changes can be observed. Figure 6d further presents the fluctuations of the repetition rate and SNR over time, with the SDs being 14.5 Hz and 0.031 dB, respectively. Here, the mode–locked fiber laser based on NPR is polarization-dependent, which results in the central wavelength being slightly affected by environmental perturbations. The above results indicate that the laser has good long—term robustness.

# 3.2. ANDi Supercontinuum Spectral Broadening

The evolution of the SC broadening spectrum of the seed pulse with the output power of pump2 is shown in Figure 7a. The spectrum is broadened from the central wavelength of 1564.5 nm to both sides with the increase of pump power. Moreover, when the pump power is less than ≈500 mW, the wavelength broadening in the shorter wavelength region is greater than that in the longer wavelength region due to SPM in the ANDi HNLF. However, further increasing the power will lead to an enhanced Raman effect and a greater broadening of the long wavelength region. To further study the characteristics of SC, a 3D pseudocolor image of the broadened spectrum is shown in Figure 7b. There is an obvious peak at 1532 nm, and the spectrum gradually becomes uneven with the increase of pump power. To increase the peak power of the pulse, the width needs to be further compressed so that the seed pulse can effectively excite nonlinearity to achieve spectrum broadening. Figure 7c shows the autocorrelation trace of the compressed pulse, whose half-maximum full width (FWHM) is 336 fs, corresponding to a pulse duration of about ≈207 fs (assuming a sech pulse shape). The spectral bandwidth with increasing pump power is characterized. The 3 dB bandwidth first increases and then decreases, while the 10 dB bandwidth increases continuously, which indicates that the spectrum continues to widen with the increase of power, but the spectrum is not flat any more when the pump power reaches 620 mW, as shown in Figure 7d. Figure 7e shows the amplified spontaneous emission (ASE) spectrum of ESF and the broadened spectrum at a specific pump power. The ASE effect will increase with increasing the pump power, and the 1532 nm peak originates from ASE. When the pump power is set to 620 mW, the spectrum spans the S-band, C-band and L-band (1490–1610 nm), and a flat ultra-broadband spectrum with a 3 dB and 10 dB spectral bandwidths of 86.4 nm and 120 nm, respectively, are obtained as shown in Figure 7f.

The SC source is injected into the time-stretching system, and the single-shot spectrum is obtained by DFT. Then the energy and cross-correlation distribution between the single-shot spectra are statistically characterized. The single-shot spectral evolution of SC with the pump power of 620 mW is shown in Figure 8a. Here, the spectral shape of the pulse has no obvious intensity fluctuation, indicating that SC broadening maintains SP operation with good repeatability. The average result of the single-shot DFT spectrum of 3586 round trips is compared with the spectrum obtained by OSA, as shown in Figure 8b. The DFT spectrum is in a good agreement with the OSA spectrum, and the slight difference is due to insufficient averaging and the deviation of the DCF dispersion curve. The above results show that the DFT spectrometer can accurately measure the SC broadening spectrum. Additionally, the energy stability of single-shot spectrum is an important index to evaluate the performance of SC-based swept source. Figure 8c presents the normalized spectral energy distribution with round trip, and the energy fluctuation is between 0.987 and 0.994. The energy fluctuation range of a single-shot spectrum is only 0.7%, indicating that the swept source formed by the time-stretched SC pulse has high periodic repeatability

nditions) on Wiley Online Library for rules of use; OA articles are governed by the applicable Creative Commons License

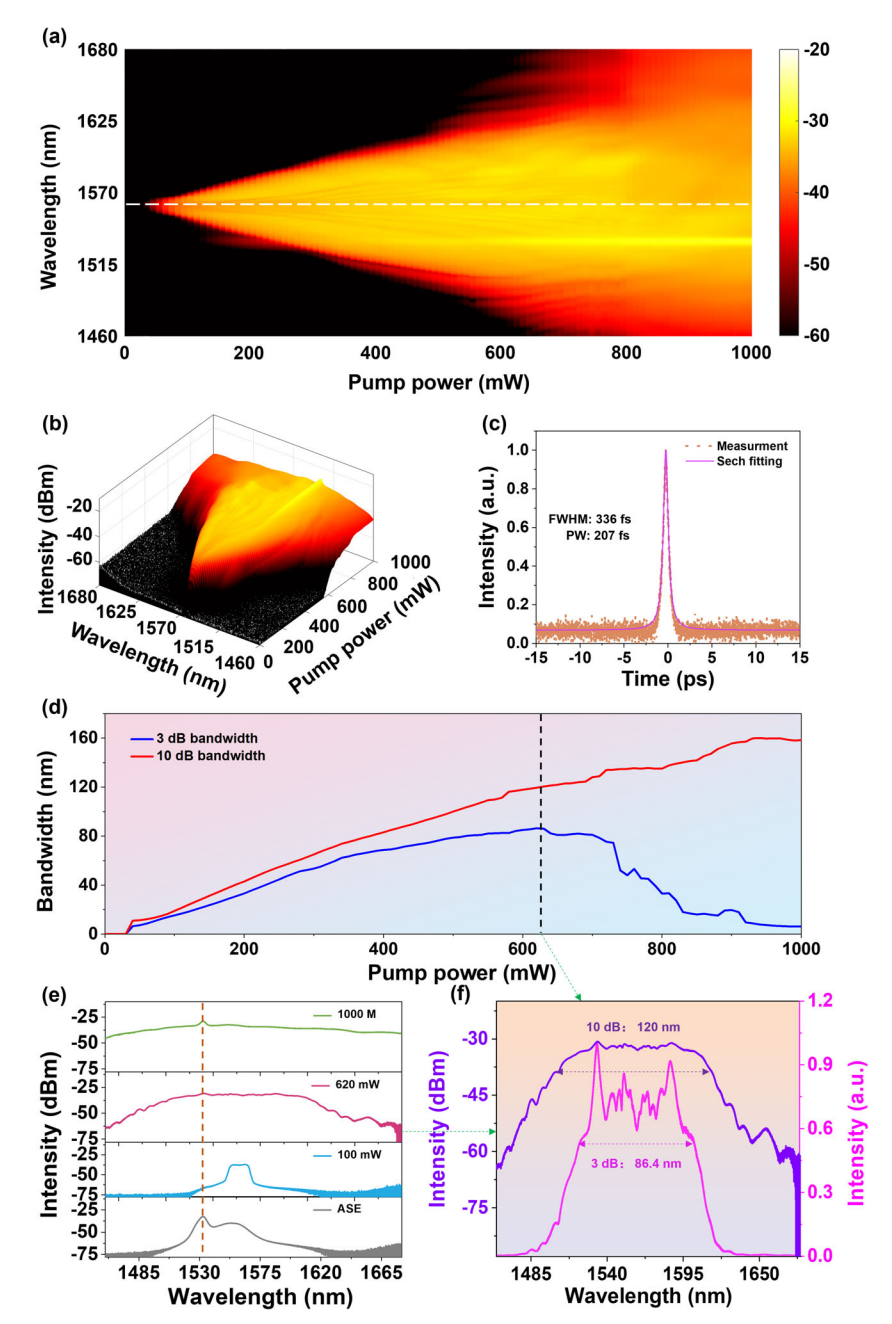


Figure 7. Characterization of supercontinuum broadening properties. a) Spectra measurements for varying pump power of broadening system. b) 3D pseudo—color image of the broadened spectrum evolving with pump power. c) Measured autocorrelation trace of the seed pulse after the compression stage. d) Evolution of the spectral bandwidth versus pump power. e) Comparison of the ASE spectrum and the broadened spectrum for individual specific pump powers. f) Spectra in logarithmic and linear scales at 620 mW pump power.

and high stability. The histograms of energy fluctuations of 3586 spectra are further counted, as shown in Figure 8d. The spectral energy concentration is 0.99, and the coefficient of variation std/mean is 0.11%, indicating that SC broadening has low energy fluctuation. To measure the noise level of the SC source, the relative intensity noise is further measured, as shown in Figure 8e. The RIN measured in the frequency offset range above 1 MHz is  $-128~{\rm dB~Hz^{-1}}$ , lower than the  $-125~{\rm dB~Hz^{-1}}$  of the seed source (see Figure 3b), and the low frequency noise present in the seed

source is also suppressed. The ANDi broadening system used can achieve flat spectral broadening with shot—noise limited performance. To further verify the similarity of the single—shot spectrum, the 2D map of the full spectral cross—correlation coefficient is calculated, as shown in Figure 8f. The higher the spectral similarity, the closer the cross—correlation coefficient is to 1. Here, the cross—correlation value gradually degenerates from the 45° diagonal line outward. To explore the degradation law and level in detail, the spectral correlation curve with a round—trip

18638899, 0, Downloaded from https://onlinelibrary.wiley.com/doi/10.1002/por.202500743 by HONG KONG POLYTECHNIC UNIVERSITY HU NG HOM, Wiley Online Library on [30.09/2025]. See the Terms

-and-conditions) on Wiley Online Library for rules of use; OA articles are governed by the applicable Creative Commons

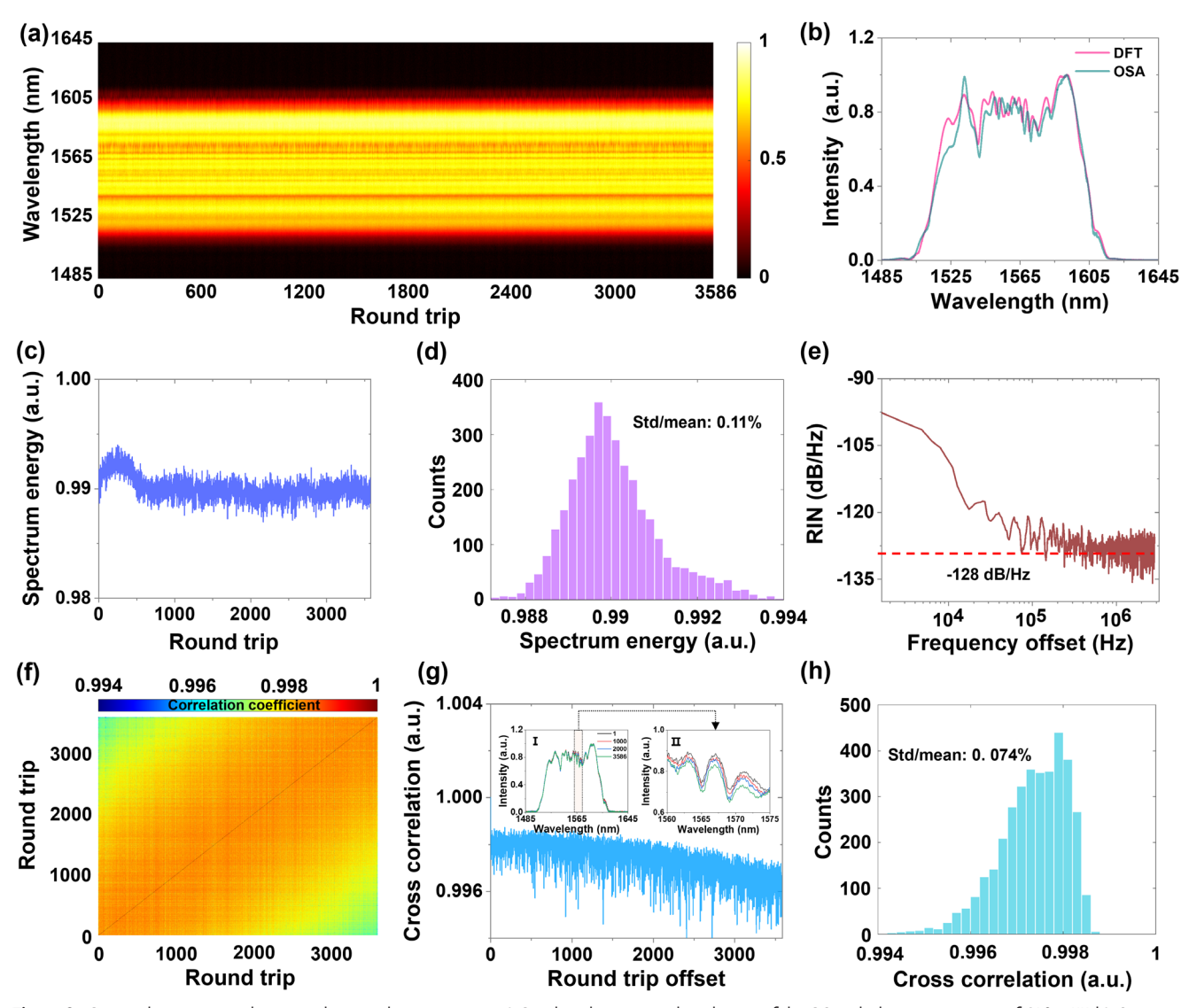


Figure 8. Spectral cross—correlation and noise characteristics. a) Single—shot spectral evolution of the SC with the pump power of 620 mW. b) Comparison of the average spectra obtained by DFT and OSA. c) Single—shot spectral energy evolutions with round trip. d) Histogram of single-shot spectrum energy within 3586 round trips. e) RIN curve of the SC source. f) Evolution of the cross—correlation coefficient between single—shot spectra. g) Spectral correlation curve within the round—trip offset of 3586, illustrations present shot—to—shot spectra and zoom-ins of different round trips. h) Histogram of the autocorrelation coefficient count distribution.

offset number ranging from 0 to 3586 is calculated, as shown in Figure 8g. It can be obtained that the cross—correlation coefficients of the spectra in different round-trip periods vary between 0.994 and 0.998, indicating that the spectra of the time—stretched SC pulses are highly similar. To compare the repeatability of the shot—to—shot spectra in detail, single—frame spectra of different round trips are further measured, as shown in the inset I of Figure 8g. It can be obtained that the single—frame spectrum of the supercontinuum has relatively good repeatability and consistency. However, the intensity of the spectrum decreases as the round trip increases within the wavelength range of 1560 nm to 1575 nm, the inset II of Figure 8g. Hence, the spectral correlation coefficient will gradually decrease with the increase of

round trips. This wavelength region precisely corresponds to the 10 dB bandwidth range of the seed laser. The reason for this phenomenon is that the seed laser power is reduced. After the laser is stabilized, this effect can be eliminated, and the supercontinuum performance can be further improved. Figure 8h statistics the histogram of the cross–correlation coefficient distribution of single–frame spectra corresponding to different round trips, and the values are distributed around  $\approx 0.997$ . Moreover, the ratio of the standard deviation to the mean (std/mean) of the correlation is calculated to be only 0.074%. The results show that the spectra between different scanning periods have high similarity, verifying that the SC–based swept laser has high coherence with low noise.



www.advancedsciencenews.com

LASER & PHOTONICS REVIEWS

www.lpr-journal.org

#### 3.3. SS-OCT Imaging with Long Detection Range

The swept source plays a crucial role in the SS-OCT system. The larger sweep range will achieve higher axial resolution of imaging, higher coherence will increase the detection distance, and a higher sweep rate will realize faster imaging. Therefore, it is very important to develop a swept source with broadband sweep range, high coherence, and high sweep rate. Generally, the coherence length of the time-stretched swept source is much larger than the actual imaging range due to the limited bandwidth of the photodetector. In theory, the axial resolution of OCT imaging can be expressed as

$$\delta z = \frac{2\ln 2}{\pi} \frac{\lambda_0^2}{n_{\text{eff}} \Delta \lambda} \tag{1}$$

where  $\lambda_0$  is the central wavelength,  $\Delta\lambda$  is the sweep range and  $n_{\it eff}$  is the effective refractive index. It is worth noting that the higher the sweep rate, the greater the bandwidth of the detector required for the same imaging range, and there is a trade–off. The specific expression is as follows:

$$\delta v_B = \frac{2n_{eff}\gamma_S z}{c} \tag{2}$$

where  $\delta v_B$  is the bandwidth of the detector,  $\gamma_S$  is the sweep rate, z is the imaging range, and c is the speed of light in a vacuum. Therefore, the introduction of a swept source with MHz–level sweep rate in OCT systems can reduce the requirements on detection equipment and improve the imaging distance while ensuring high–speed imaging.

Here, the swept source is constructed by a self-built low repetition rate mode-locked laser with shot-noise limited supercontinuum broadening assisted by time stretching. The swept source has a high sweep rate of 5.7 MHz and a flat broadband sweep range with a 3 dB bandwidth of 86.4 nm and 10 dB bandwidth of 120 nm. As a result, long detection range, high A-scan axial resolution and fast imaging can be achieved in an SS-OCT system. The performance characterization of the SS-OCT system is performed using a single reflective mirror at the sample location, as shown in **Figure 9**. The different wavelength components of the pulse are obviously separated in the time domain, which proves that the time-stretched signal has wavelength sweeping characteristics. Figure 9a measures the mapping relationship between each wavelength of the pulse signal and the time position. Here, a quadratic polynomial fitting is performed on the swept trace. The corresponding total dispersion parameter and coefficient can be obtained according to the fitting parameters as -1050 ps nm<sup>-1</sup> and 0.7968 ps nm<sup>-2</sup>, which are consistent with the dispersion amount brought by the 6.5 km DCF. Therefore, it can be obtained that the time-stretched swept source is implemented by the second-order dispersion in DCF. According to the normal dispersion of DCF, the scanning is from the long wavelength to the short wavelength region. The interference signal obtained by the SS-OCT system is shown in Figure 9b, where the interference fringes are not uniform. Therefore, it is necessary to use the swept trace to resample in the frequency domain to achieve homogenization. The stability of the swept trace determines the accuracy of resampling. Here, the proposed swept source has low noise and high stability, and then there is no need to set the starting point of the sampling cycle many times in the experiment. Then, the point spread function (PSF) of the imaging system can be obtained by using fast Fourier transform after resampling the signal, as shown in Figure 9c. By fitting the PSF with a Gaussian profile, the axial resolution of the A-scan in air can be as high as 11.4 µm benefitting from the flat broadband spectrum of the swept source. By measuring the PSFs of different delays between the reference and sample arms in the OCT system, the imaging range and quality of the OCT system can be explored. The PSFs measured at different VODL lengths are shown in Figure 9d. Here, a Gaussian envelope is generated by applying a window function to the collected interference signal to suppress sidelobes. Predictably, the imaging ranges are as high as 119 and 137 mm, with corresponding sensitivity roll-offs of 6 and 7.4 dB, which are the longest detection ranges of MHz-level SS-OCT system reported so far. A longer imaging distance can be measured based on the 10 dB sensitivity roll-off, which is limited by the maximum adjustable length of VODL. In Figure 9d, the SNR of PSFs can reach ≈42 dB, which is higher than the typical SNR of 40 dB for SS-OCT system. Therefore, the above results prove that reducing the sweep rate of the time-stretched swept source can improve the performance of SS-OCT imaging. Then, to further illustrate the high axial resolution characteristics of the OCT system, three overlapping plastic plates with rough surfaces are imaged. As shown in Figure 9e, the three layers of plastic plates can be clearly identified, corresponding to the two reflective surfaces of the 0.5 mm thick plastic plate, and different reflection intensities are also clearly detected. In addition, an air layer formed by a piece of tape is placed between the first and second plastic plates, and the burs on the surface can also be clearly identified.

# 4. Discussion

The parameter space of time-stretched swept source-assisted SS-OCT calculations is further discussed in detail, as shown in Figure 10. In Figure 10a, the evolution of axial resolution with sweep range according to Equation 1 with fixed  $\lambda_0 = 1550$  nm is plotted. The higher axial resolution can be obtained by increasing the sweep range. Therefore, the spectrum of the mode-locked laser is broadened to realize high axial resolution by using shot-noise limited SC in our OCT system. The theoretical axial resolution in air is marked by a red pentagram as  $8.83~\mu m$ . The difference between the theoretical and experimental axial resolution is caused by the asymmetry of spectral profile and the resampling error of wavelength to time domain mapping. Referring to Equation 2, we map the imaging range as a function of detector (OSC or PD) bandwidth and pulse repetition rate, as shown in Figure 10b. Herein, the reduction of repetition rate and the increase of detection bandwidth can result in a long imaging range. In our experiment, we set the laser repetition rate to be 5.767 891 MHz, the detection bandwidth to be 70 GHz, and the corresponding theoretical imaging range is 121 mm, which is in good agreement with the 6 dB sensitivity roll-off of 119 mm. Generally, the electronic detection bandwidth is limited, and large detection bandwidth will cause high cost, which is not practical to real applications. As a result, a larger imaging range can be obtained by reducing the repetition rate, ultimately en-

18538899, 0, Downloaded from https://onlinelibrary.wiley.com/doi/10.1002/por.202500743 by HONG KONG POLYTECHNIC UNIVERSITY HUNG HOM, Wiley Online Library on [30.09/2025]. See the Terms

and-conditions) on Wiley Online Library for rules of use; OA articles are governed by the applicable Creative Commons License

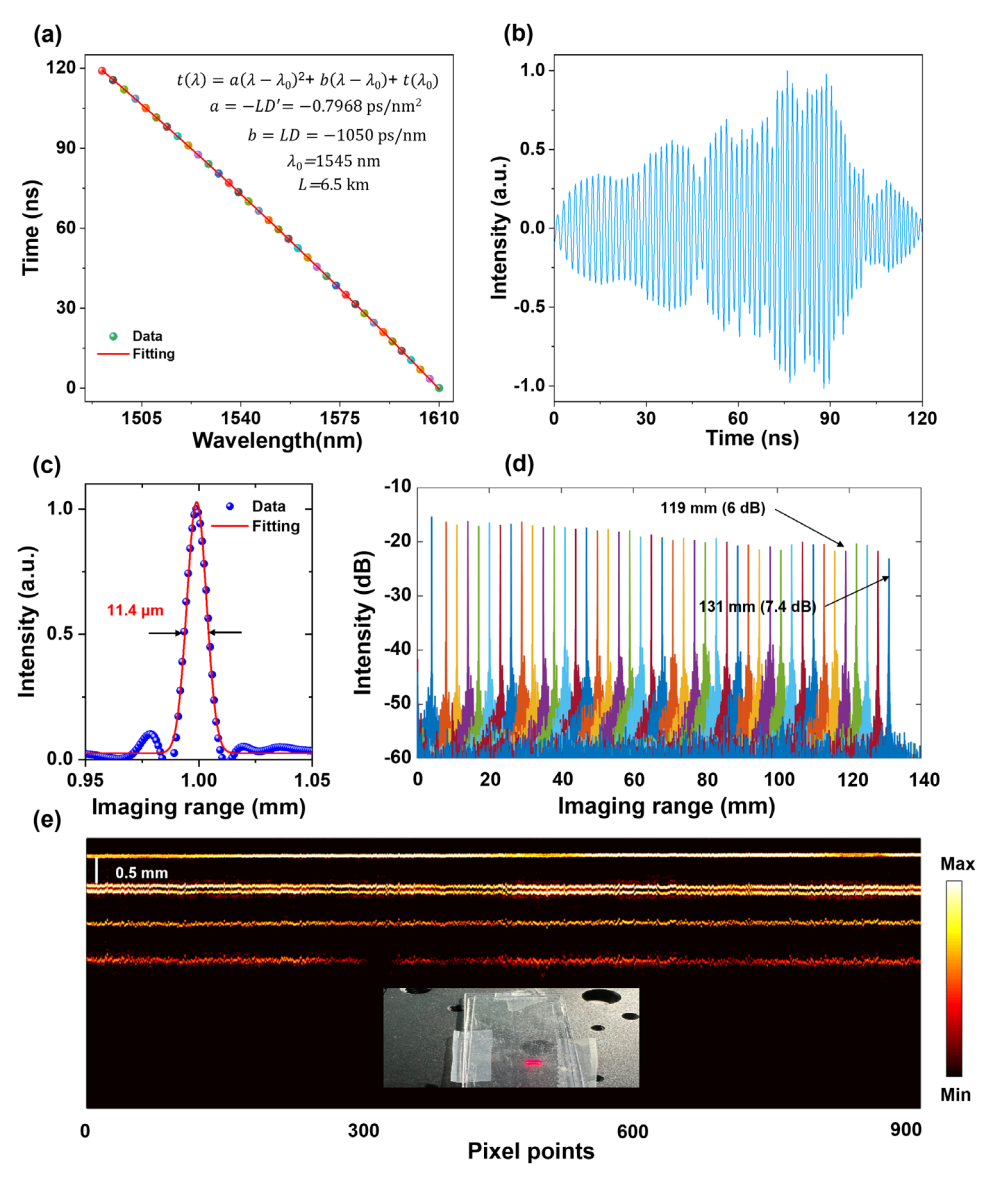


Figure 9. Performance of the OCT system driven by a 5.7 MHz swept source. a) Swept trace of the time-stretched SC source from 1490–1610 nm. b) Single frame scanning interference signal. c) Axial resolution of A-scan in air. d) Sensitivity performance of roll-off with increased VODL. e) OCT imaging of three stacked roughened plastic plates.

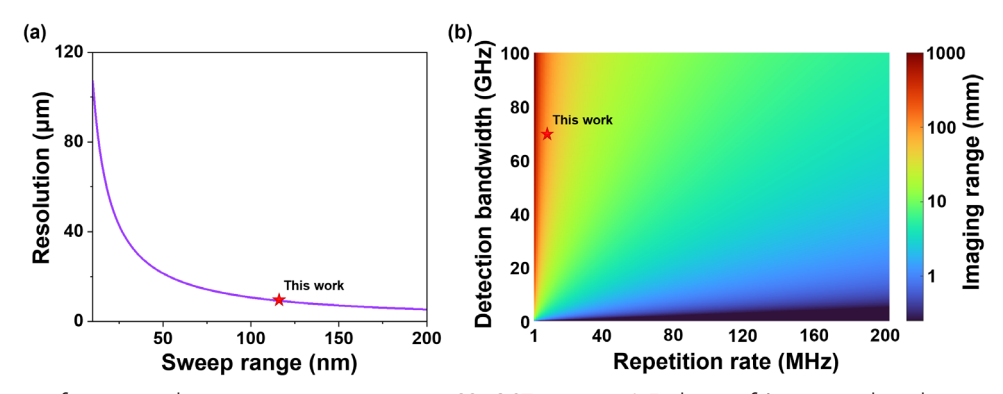


Figure 10. Limitations of time-stretch swept source parameters on SS-OCT imaging. a) Evolution of A-scan axial resolution with sweep range. b) Laws of imaging range with laser repetition rate and detection bandwidth.

.com/terms-and-conditions) on Wiley Online Library for rules of use; OA articles are governed by the applicable Creative Commons

www.advancedsciencenews.com

www.lpr-journal.org

abling long imaging range, high resolution, and fast OCT imaging.

# 5. Conclusion

In this work, the combination of LMAF in the long cavity is first investigated, which provides a novel scheme to engineer the dispersion and nonlinearity inside the laser cavity to generate MHz repetition rate stable mode locked pulse. The low repetition stable mode locked laser is used as the seed laser to generate SC with low noise and high coherence by pumping the ANDi fiber. By time stretching technology, we have demonstrated a high performance swept laser with a sweep rate of 5.7 MHz, 3 dB, and 10 dB bandwidths of 86.4 and 120 nm, respectively. The RF spectrum of the seed mode locked laser has a SNR of up to 92.4 dB, and the pulse duration can be compressed to 207 fs, with self-starting and long-term stability. The RIN of the SC source is as low as −128 dB Hz<sup>-1</sup>, and the spectral correlation coefficients between different round trips are greater than ≈0.994. The short-noise limited SC is time-stretched to generate a swept signal and applied to the SS-OCT system. An imaging range with 6 dB sensitivity roll-off length is up to 119 mm and a high axial resolution is 11.4 µm, which is further applied for a clear imaging of the microstructures of three coated plastic plates. This is the first time that the 6 dB sensitivity roll-off length of SS-OCT has been increased to more than 110 mm directly through an all-fiber system without compromising axial resolution. The achievements will accelerate innovation and breakthroughs in time stretched swept lasers and boost their applications in high speed, high resolution, and long-distance spectral detection, including optical frequency domain reflectometer, swept source optical coherence tomography, and LiDAR.

# Acknowledgements

L.D. and W.Z. contributed equally to this work. This work was supported by the Research Grants Council, University Grants Committee of Hong Kong SAR (PolyU 15206023), the Innovation and Technology Fund–Guangdong–Hong Kong Technology Cooperation Funding Scheme (GHP/096/22SZ), the PolyU Postdoc Matching Funding Scheme (P0045822) and the Shenzhen–Hong Kong Joint Research Project (SGDX20230116093302005).

#### Conflict of Interest

The authors declare no conflict of interest.

# **Data Availability Statement**

The data presented in the manuscript are available from the corresponding author upon reasonable request.

#### Keywords

all-normal dispersion, low-repetition-rate, optical coherence tomography, supercontinuum broadening, swept-sources

Received: April 2, 2025 Revised: May 21, 2025 Published online:

- [1] M. O. Ko, S.-J. Kim, J.-H. Kim, B. W. Lee, M. Y. Jeon, Opt. Express 2014, 22, 16139.
- [2] J. Qin, L. Zhang, W. Xie, R. Cheng, Z. Liu, W. Wei, Y. Dong, Opt. Express 2019, 27, 19359.
- [3] T. Klein, W. Wieser, L. Reznicek, A. Neubauer, A. Kampik, R. Huber, Opt. Express 2013, 4, 1890.
- [4] D. C. Adler, Y. Chen, R. Huber, J. Schmitt, J. Connolly, J. G. Fujimoto, Nat. Photonics 2007, 1, 709.
- [5] M. Okano, C. Chong, Opt. Express 2020, 28, 23898.
- [6] Y. Jiang, S. Karpf, B. Jalali, Nat. Photonics 2020, 14, 14.
- [7] M. Siddiqui, A. S. Nam, S. Tozburun, N. Lippok, C. Blatter, B. J. Vakoc, Nat. Photonics 2018, 12, 111.
- [8] T. Klein, R. Huber, Biomed. Opt. Express 2017, 8, 828.
- [9] B. Baumann, B. Potsaid, M. F. Kraus, J. J. Liu, D. Huang, J. Hornegger, A. E. Cable, J. S. Duker, J. G. Fujimoto, *Biomed. Opt. Express* 2011, 2, 1539
- [10] M. P. Minneman, J. Ensher, M. Crawford, D. Derickson, Asia Communications and Photonics Conference 2011, 831116.
- [11] J. Zhang, T. Nguyen, B. Potsaid, V. Jayaraman, C. Burgner, S. Chen, J. Li, K. Liang, A. Cable, G. Traverso, H. Mashimo, J. G. Fujimoto, Biomed. Opt. Express 2021, 12, 2384.
- [12] V. Jayaraman, G. D. Cole, M. Robertson, C. Burgner, D. John, A. Uddin, A. Cable, Electron. Lett. 2012, 48, 21.
- [13] R. Huber, M. Wojtkowski, J. G. Fujimoto, Opt. Express 2006, 14, 3225.
- [14] D. Huang, Y. Shi, F. Li, P. K. A. Wai, Sensors 2022, 22, 3145.
- [15] C. Lei, B. Guo, Z. Cheng, K. Goda, Appl. Phys. Rev. 2016, 3, 011102.
- [16] J. Xu, X. Wei, L. Yu, C. Zhang, J. Xu, K. K. Y. Wong, K. K. Tsia, Biomed. Opt. Express 2015, 6, 1340.
- [17] X. Wei, C. Kong, S. Sy, H. Ko, K. K. Tsia, K. K. Y. Wong, Biomed. Opt. Express 2016, 7, 5208.
- [18] L. R. Wang, X. M. Liu, Y. K. Gong, D. Mao, H. Feng, Laser Phys. Lett. 2011, 8, 376.
- [19] X. Li, W. Zou, G. Yang, J. Chen, IEEE Photonics Technol. Lett. 2015, 27,
- [20] G. Sobon, J. Sotor, T. Martynkien, K. M. Abramski, Opt. Express 2016, 24, 6156.
- [21] M. Michalska, Opt. Laser Technol. 2021, 138, 106923.
- [22] Z. Łaszczych, G. Soboń, Opt. Express 2021, 29, 2690.
- [23] Y. Zhou, Y. Zeng, J. Yin, T. Dong, L. Sun, Y. Zhang, K. Xu, Laser Phys 2020, 30, 045101.
- [24] J. Zhou, W. Pan, X. Fu, L. Zhang, Y. Feng, Opt. Fiber Technol. 2019, 52, 101963.
- [25] D. Huang, F. Li, C. Shang, Z. Cheng, P. K. A. Wai, *Photonics Res.* 2020, 8 1360
- [26] P. Bowen, M. Erkintalo, R. Provo, J. D. Harvey, N. G. Broderick, Opt. Lett. 2016, 41, 5270.
- [27] D. Stoliarov, E. Manuylovich, A. Koviarov, D. Galiakhmetova, E. Rafailov, Opt. Express 2023, 31, 43427.
- [28] C. Hönninger, R. Paschotta, F. Morier-Genoud, M. Moser, U. Keller, J. Opt. Soc. Am. B 1999, 16, 46.
- [29] M. Baumgartl, J. Abreu-Afonso, A. Díez, M. Rothhardt, J. Limpert, A. Tünnermann, Appl. Phys. B 2013, 111, 39.
- [30] A. Agnesi, L. Carrá, F. Pirzio, R. Piccoli, G. Reali, J. Opt. Soc. Am. B 2013, 30, 2960.
- [31] W. Chen, Y. Song, K. Jung, M. Hu, C. Wang, J. Kim, Opt. Express 2016, 24, 1347.
- [32] F. X. Kaertner, L. R. Brovelli, D. Kopf, M. Kamp, I. G. Calasso, U. Keller, Opt. Eng. 1995, 34, 2024.
- [33] A. Davis, O. Levecq, H. Azimani, D. Siret, A. Dubois, Biomed. Opt. Express 2019, 10, 694.
- [34] D. H. Martínez-Suárez, M. C. S. Araujo, D. Steinberg, L. M. A. Saito, E. T. de Souza, J. D. Zapata, Opt. Laser Technol. 2024, 174, 110588



LASER & PHOTONICS REVIEWS

www.advancedsciencenews.com www.lpr-journal.org

- [35] Y. X. Guo, X. H. Li, P. L. Guo, H. R. Zheng, Opt. Express 2018, 26, 9893.
- [36] E. Genier, P. Bowen, T. Sylvestre, J. M. Dudley, P. M. Moselund, O. Bang, J. Opt. Soc. Am. B 2019, 36, A161.
- [37] P. Abdolghader, A. F. Pegoraro, N. Y. Joly, A. Ridsdale, R. Lausten, F. Légaré, A. Stolow, Opt. Express 2020, 28, 35997.
- [38] M. Klimczak, B. Siwicki, A. Heidt, R. Buczyński, *Photon. Res.* 2017, 5, 710.
- [39] S. Grelet, A. M. Jiménez, R. D. Engelsholm, P. B. Montague, A. Podoleanu, IEEE Photonics J 2022, 14, 3963606.
- [40] H. Chen, Y. Li, D. Huang, F. Li, C. Lu, P. K. Wai, *Opt. Express* **2021**, *29*, 33322.
- [41] Y. Cui, Y. Zhang, Y. Song, L. Huang, L. Tong, J. Qiu, X. Liu, Laser Photonics Rev. 2021, 15, 2000216.
- [42] C. M. Harvey, F. Yu, J. C. Knight, W. J. Wadsworth, P. J. Almeida, IEEE Photonic. Tech. L. 2015, 28, 669.
- [43] X. Cao, J. Zhou, Z. Cheng, S. Li, Y. Feng, Laser Photonics Rev. 2023, 17, 2300537.